nature communications

Article

https://doi.org/10.1038/s41467-025-59678-2

The identification of XPR1 as a voltage- and phosphate-activated phosphate-permeable ion channel

Received: 10 December 2024

Accepted: 29 April 2025

Published online: 15 May 2025

Check for updates

Hongjiang Wu[1,7], Liang Sun[2,7], Tong Huo[1], Theodore G. Wensel[1], Frank T. Horrigan[2] ✉ & Zhao Wang[1,3,4,5,6] ✉

Maintaining a balance of inorganic phosphate (Pi) is vital for cellular functionality. Proper phosphate levels are managed through Pi import and export; and the processes governing Pi export remain the least understood. Xenotropic and Polytropic retrovirus Receptor 1 (XPR1) has been identified as the only known Pi export protein in mammals. In this study, we introduce the cryogenic electron microscopy structure of human XPR1 (hXPR1), unveiling a structural arrangement distinct from that of any known ion transporter. Our structural results suggest that hXPR1 may operate as an ion channel, a hypothesis supported by patch clamp recordings revealing hXPR1's voltage- and Pi-dependent activity and large unitary conductance. Further analyses, including the structure of hXPR1 in presence of Pi, and mutagenesis studies at one of the putative Pi binding sites, lead us to propose a plausible ion permeation pathway. Together, our results provide novel perspectives on the Pi transport mechanism of XPR1.

Xenotropic and polytropic retrovirus receptor 1 (XPR1), also known as SLC53a1 of the solute carrier (SLC) superfamily, is a multi-pass membrane protein initially identified in mice as the cell surface entrance receptor for murine xenotropic and polytropic retroviruses[1,2]. The function of XPR1 was later found to mediate inorganic phosphate (Pi) export from the cytosol to the extracellular space[3–5]. The protein is well conserved phylogenetically across all eukaryotes, and the Pi-exporting activity has been demonstrated in various orthologues[6–10].

Given the role of Pi in many key cellular processes, including energy production, biosynthesis, and cell signaling, its intracellular concentration is tightly regulated, in part through controlling Pi import and export[11,12]. XPR1 is the only known inorganic phosphate exporter in mammals, is present in most cell types[12], and thus plays a central role in maintaining cellular Pi homeostasis. XPR1 mutations have been associated in patients with primary familial brain calcification (PFBC)[4,5,13–17], a genetic neurodegenerative disorder marked by progressive bilateral calcification distributed primarily in the basal ganglia region[18]. In addition, the upregulation of XPR1 has been implicated in several cancers, facilitating cancer proliferation, migration, and invasion[19–25]. Considering the critical role of XPR1 in regulating Pi homeostasis and the current knowledge gaps in our understanding of its connection to XPR1-related diseases, a systematic study to explore its structural-functional mechanisms is of great importance.

All XPR1 homologs are composed of two major functional domains: the N-terminal cytosolic SPX (SYG1/PHO81/XPR1) domain and the transmembrane domain (TMD). The SPX domain was discovered as an intracellular phosphate sensor[26], and the XPR1-mediated Pi export activity is regulated by SPX binding to inositol polyphosphates[27–29]. Secondary structure predictions proposed that the XPR1 TMD is composed of 8 transmembrane α-helices[4]. Part of the TM region belongs to the EXS (ERD1/XPR1/SYG1) domain family, which

[1]Verna and Marrs McLean Department of Biochemistry and Molecular Pharmacology, Baylor College of Medicine, Houston, TX, USA. [2]Department of Integrative Physiology, Baylor College of Medicine, Houston, TX, USA. [3]Department of Molecular and Cellular Biology, Baylor College of Medicine, Houston, TX, USA. [4]CryoEM Core (Advanced Technology Core), Baylor College of Medicine, Houston, TX, USA. [5]Department of Materials Science and NanoEngineering, Rice University, Houston, TX, USA. [6]Department of Molecular and Cellular Oncology, Division of Basic Science, The University of Texas MD Anderson Cancer Center, Houston, TX, USA. [7]These authors contributed equally: Hongjiang Wu, Liang Sun. ✉e-mail: horrigan@bcm.edu; zhaow@bcm.edu

was demonstrated to be essential for proper localization to the plasma membrane and Pi export activity for the plant orthologue PHO1[30]. Whereas crystal structures have been reported for the SPX domain[26], a detailed structure-function relationship study of the full-length XPR1 protein could enhance the understanding of the transport mechanism of XPR1 and its critical role in regulating phosphate homeostasis. In this study, we present the cryo-EM structures of full-length human XPR1 and demonstrate that it functions as a voltage- and Pi-dependent ion channel permeable to Pi.

Results

Cryo-EM structure of hXPR1

We expressed full-length human XPR1 (hXPR1) in HEK293S GnTI$^-$ cells, purified the protein in a detergent mixture (Supplementary Fig. 1), and determined the structure by cryogenic electron microscopy single particle analysis (cryo-EM SPA) in the absence of any Pi or known ligands. The overall resolution of the apo-hXPR1 (ligand-free) map reached 3.4 Å with the transmembrane region extended to 2.7 Å. The quality of the map was sufficient to allow accurate assignments of backbones and side chains within the TMD (Supplementary Figs. 2 and 4a). The cytosolic domain of apo-hXPR1 was relatively poorly resolved compared to the TMD, possibly due to flexibility, but we were able to perform rigid body docking and flexible fitting to accommodate the previously determined SPX crystal structure[26] (PDB:5IJH) into the density map. The identification of the position of the SPX domain enables the unambiguous assignment of TMD topology.

hXPR1 in a detergent mixture forms a homodimer. The overall TM domain has a trapezoidal shape with dimensions of 110 × 40 × 50 Å (Fig. 1a and Supplementary Movie 1). For each protomer, the cytosolic SPX domain connects to the TMD via an unresolved flexible linker, and the C-terminus is situated in the cytosol as well (Fig. 1b). The TM domain of each protomer consists of 10 transmembrane α-helices as opposed to 8 helices hypothesized previously (Fig. 1b, c). The dimeric interaction is mediated predominantly within the TM region by TM1, and the dimer interface has a buried surface area of 449 Å^2. It is interesting to note that the previously predicted EXS domain, which was hypothesized to contain a long cytoplasmic loop and three TM helices, spans the TM5 to TM10 segments with the predicted loop amounting to TM6 and TM7 (Fig. 1b). There are 4 long intracellular loops connecting TM2 to TM3, TM4 to TM5, and TM8 to TM9, and the C-terminal region is also intracellular. The only substantial extracellular loop connects TM5 to TM6 (Fig. 1c).

It was previously reported that XPR1 adopts a unique fold compared to other members of the SLC family[31]. To determine if the helix arrangement of the TM domain belongs to any other known structural fold, which might potentially provide insight into the Pi transport mechanism, we used the structure similarity search engine DALI[32] to compare the TM domain structure of hXPR1 to known proteins in the Protein Data Bank. Strikingly, the result indicated that the hXPR1 is not similar to any known Pi transporters or any other secondary transporters with "alternating-access" mechanisms in general[33]. This structural distinction from ion transporters suggests hXPR1 could potentially mediate Pi permeation via an uncommon mechanism. The closest resemblance of hXPR1 is to the archaeal ion-translocating rhodopsin family, where the topological arrangement of TM5-10 from hXPR1 loosely matches to TM2-7 from a light-driven chloride ion-pumping rhodopsin[34] (Supplementary Fig. 5). Such structural similarity suggests that TM5-10 might carve out an isolated space from the membrane lipid environment that creates a pathway for ion permeation, as seen in ion-translocating rhodopsin with its TM2-7. In addition, the absence of any blockade (e.g., retinal) within this isolated space may allow a continuous path, which could potentially facilitate passive diffusion as seen with ion channels.

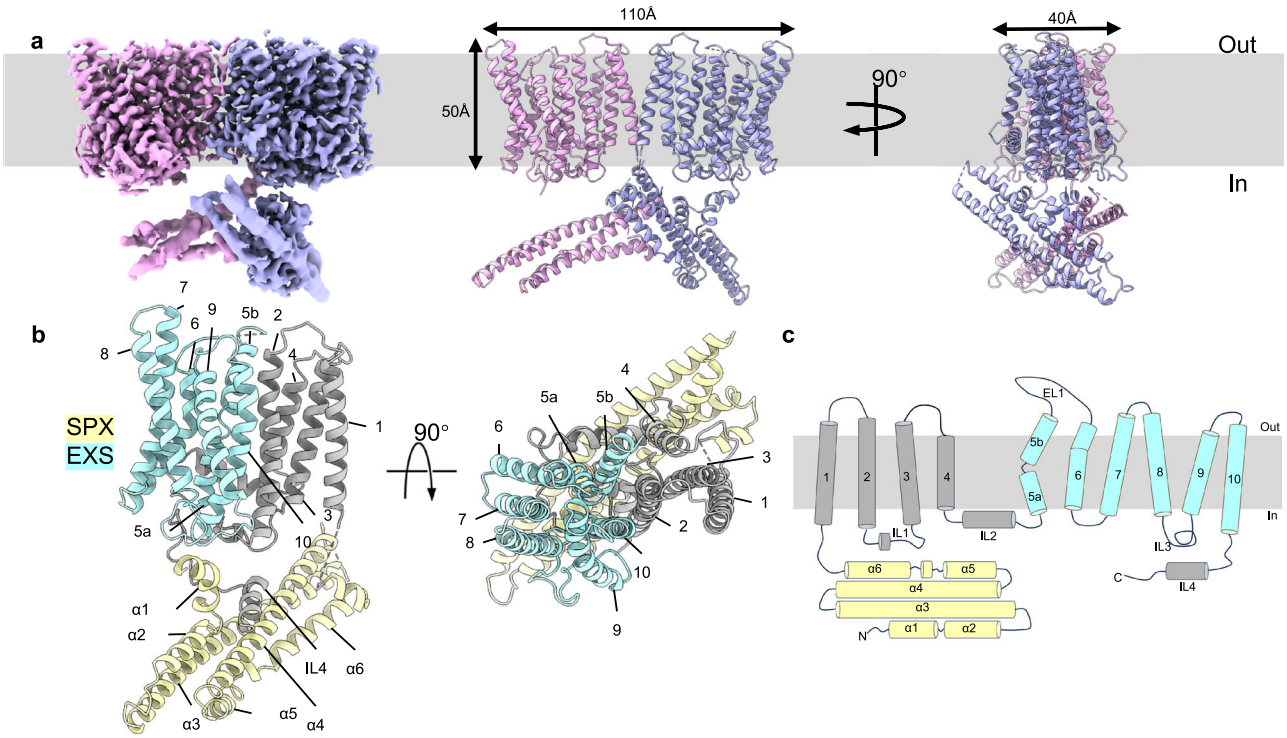

Fig. 1 | Overall structure of apo-hXPR1. a The composite Cryo-EM density map (left) and cartoon representations of the atomic model (middle and right) of apo-hXPR1 dimer viewed in the membrane plane from two orthogonal directions. Two protomers are colored magenta and lavender. The densities of the cytosolic domain and TMD are displayed at a contour level of 8.17σ and 5.04σ, respectively. The gray box in the background indicates the membrane bilayer. **b** Cartoon representations of an hXPR1 monomer viewed from the side and from top-down. The SPX domain is colored in yellow, the EXS domain in light blue, and the rest of the protein in gray. **c** Topology of a monomeric hXPR1.

https://doi.org/10.1038/s41467-025-59678-2

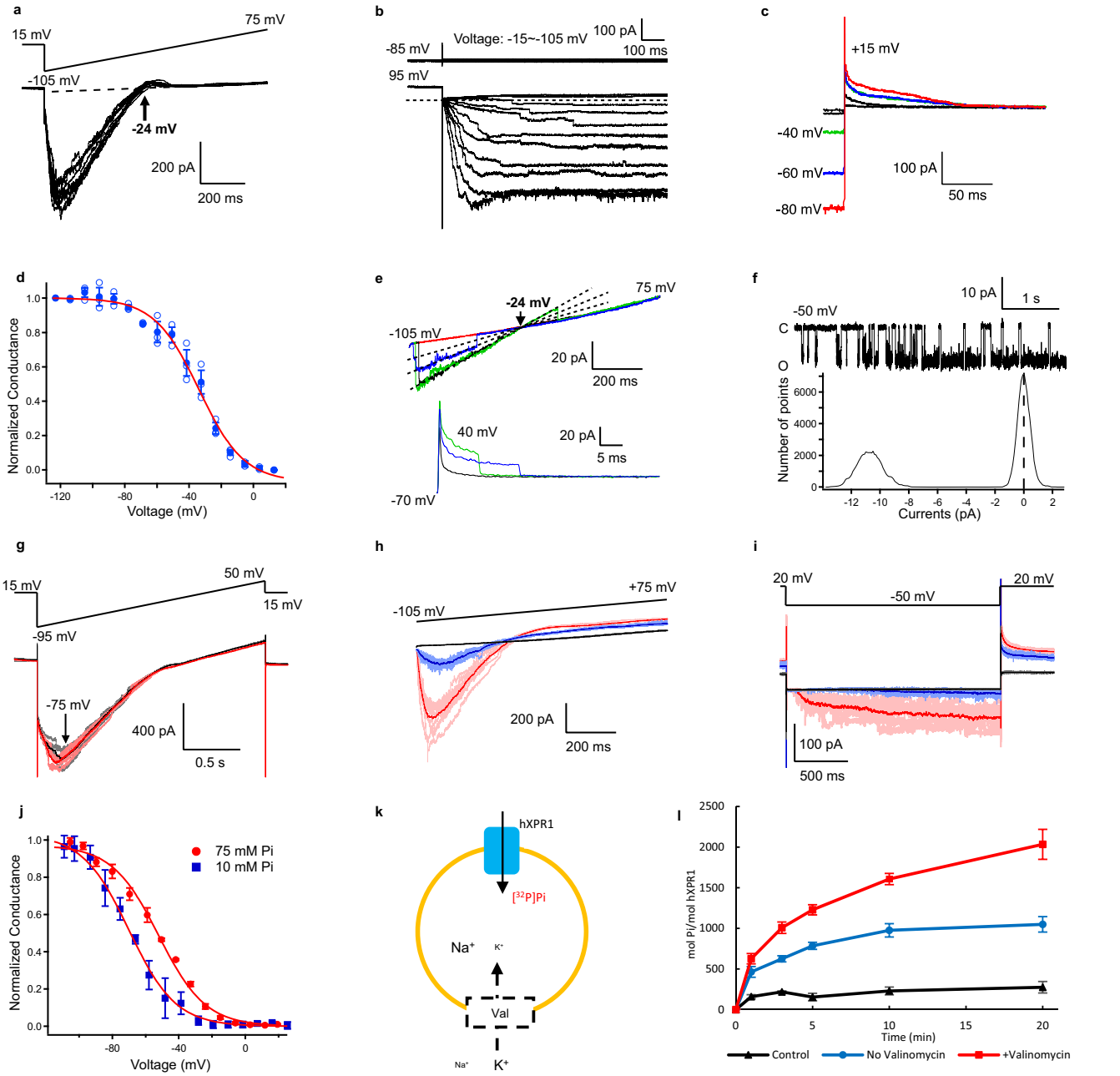

Fig. 2 | XPR1 exhibits voltage- and Pi-dependent ion channel activity and Pi transport. a Inwardly-rectifying currents evoked from an excised GUV patch with hXPR1 by voltage ramps (−105 mV to +75 mV) from +15 mV. **b** Inward currents are evoked by hyperpolarizing voltage-pulses (−15 to −105 mV, in 10 mV intervals) from +95 mV in a GUV patch with hXPR1, but not in detergent control. **c** Outward tail current at +15 mV following 1 s hyperpolarizing pulses. **d** Normalized hXPR1 G-V relation from tail currents (mean ± SEM, $n = 3$ replicates from one GUV) fit by a Boltzmann function ($z = -1.8 \pm 0.2$ *e*, $V_{1/2} = -34 \pm 2$ mV, mean ± SD). **e** Unitary current activity during voltage ramps or +40 mV pulses from a HEK293S GnTI⁻ cell expressing hXPR1. **a**–**e** were from inside-out patches with external 0 Pi NMDG-MSA and internal 20 Pi, 0.07 Ca^{2+}, K-MSA solutions. **f** Unitary XPR1 current recorded from HEK293 cell with single open level and associated all-points histogram at −50 mV with external 1 Pi NMDG-citrate and internal 20 Pi, 0.07 Ca^{2+}, K-MSA solutions. **g** XPR1 currents evoked from a GUV patch by voltage ramps with 75 mM Pi as the sole internal anion (black) or with 75 mM Pi + 10 Cl^- (red) are superimposable. XPR1 currents evoked from a GUV patch by voltage ramps (**h**) or −50 mV pulses (**i**) are enhanced as internal Pi is increased from 10 mM (blue) to 75 mM (red), and almost undetectable in 0 Pi (black) using internal 10 Cl K-MSA with external 0 Pi NMDG-MSA solutions. Thick curves represent an average of 5 (**g**) or 10 (**h**, **i**) traces (thin curves). **j** G-V relations in 10 and 75 mM Pi (mean±SEM, $n = 3$ patches). G-Vs at both [Pi] were normalized to the maximal conductance in 75 mM Pi. **k** Schematics of the [^{32}P] Pi transport assay with proteoliposomes. A membrane voltage potential difference was generated using a potassium gradient and valinomycin. **l** Time-dependent accumulation (mean±SEM, $n = 6$ independent assays) of [^{32}P] Pi in hXPR1-containing proteoliposomes without valinomycin (blue), with valinomycin (red), and in empty liposomes with valinomycin (black) as control.

hXPR1 exhibits voltage- and Pi-dependent ion channel activity, and Pi transport activity

To further investigate the ion channel hypothesis, patch clamp electrophysiology experiments were conducted using giant unilamellar vesicles (GUVs) reconstituted with purified hXPR1. Macroscopic currents recorded from excised inside-out patches in response to voltage ramps exhibited a strongly rectifying behavior with large 0.5 nA inward currents at voltages near −100 mV but little or no current at positive voltages (Fig. 2a). Inward currents evoked by 1 s pulses to different voltages following a prepulse to +95 mV activate to a steady

state, with faster activation at more negative voltages (Fig. 2b, lower panel). Small steps and stochastic fluctuations in current are evident, suggestive of ion channel activity. Importantly, control experiments lacking hXPR1, but with the same concentration of detergent, exhibited no appreciable current over the same voltage range and ionic condition (e.g., Fig. 2b, upper panel). Transient outward (tail) hXPR1 currents could be evoked by stepping to +15 mV following activation of inward current at negative voltages (Fig. 2c). The voltage-dependence of steady-state activation (Fig. 2d) was determined by plotting the mean normalized conductance-voltage relation (G-V), measured from the tail current amplitude following 1 s pulses to different voltages, and is fit by a Boltzmann function with apparent charge of −1.8 *e* and half-activation voltage of −34 mV. A similar voltage-dependence of macroscopic current was observed in whole cell recording of HEK293S cells transfected with hXPR1 (Supplementary Fig.6a, b). This voltage-dependence implies that the tail current decay at +15 mV reflects deactivation (i.e., channel closure) and that the rectifying behavior observed with voltage ramps is due to voltage-dependent channel gating as opposed to a strong dependence of open channel conductance on voltage. The latter is evident from hXPR1 currents recorded from excised patches from XPR1-expressing HEK293S cells during voltage ramps (Fig. 2e, upper panel), which reproduce the rectifying behavior in GUVs (Fig. 2a) but with an order of magnitude smaller current and stochastic activity consistent with a small number of channels. Dashed lines indicate three open levels of equal conductance, whereas the red trace with no current fluctuations represents a sweep where channels remained closed. Stochastic closing events can also be observed following steps to +40 mV (Fig. 2e, lower panel), and a different patch shows steady-state activity at −50 mV with the corresponding all-points histogram (Fig. 2f). The linear relation between current and voltage indicates that the conductance of the open channel is voltage-independent with a unitary conductance of 134 pS, based on the difference in slopes of the dashed lines in Fig. 2e.

The negative reversal potential of XPR1 current (Fig. 2a–e; arrows) indicates that the channel is not selective for Pi, as the intracellular and extracellular solutions contained 20 mM and 0 Pi, respectively. However, this observation does not rule out the possibility that the channel conducts Pi together with other ions. Indeed, large inward currents were recorded with 75 mM Pi as the sole internal anion (Fig. 2g), supporting that XPR1 is permeable to Pi. In addition, increasing internal Pi from 10 to 75 mM greatly increased peak current during voltage ramps or −50 mV pulses (Fig. 2h, i) without altering unitary current amplitude at −50 mV (Supplementary Fig. 6c–e). This indicates that XPR1 channel activity is Pi-dependent. The enhanced activity of XPR1 in 75 mM Pi is due to an 18 mV shift in the steady-state G-V relation to more positive voltages relative to 10 mM Pi without change in maximal conductance (Fig. 2j), as well as a speeding of activation kinetics (Supplementary Fig. 6c). Small macroscopic XPR1 currents could also be recorded in 0 Pi (Supplementary Fig. 6c) but only at voltages more negative than −70 mV suggesting a further difference in the voltage-dependence of activation between 0 and 10 mM Pi. Unitary current fluctuations at −75 mV in 0 Pi (Supplementary Fig. 6f) were comparable in magnitude to those observed in 10 or 75 mM Pi at −50 mV, implying that the small macroscopic XPR1 current in 0 Pi (Supplementary Fig. 6c) reflects a low open probability and failure to maximally activate the channel at the most negative voltages tested.

XPR1 does not appear to be selective for Pi versus methanesulfonate. The currents recorded in 0 Pi, with methanesulfonate as the primary internal anion, indicate that the channel is permeable to this ion. Furthermore, the change from 75 mM to 10 mM Pi, which involved substitution of 100 mM methanesulfonate for Pi, had no appreciable effect on the unitary current amplitude (Supplementary Fig. 6d, e). The internal solution for this experiment also included 10 mM Cl^-. However, switching from 0 to 10 mM Cl^- in the presence of 75 mM Pi had no effect on mean current amplitude following XPR1 activation (arrow Fig. 2g), implying that Cl^- at this low concentration makes little or no contribution to XPR1 conductance. The selectivity of the channel was not investigated in detail owing in part to the strong dependence of channel activity on internal [Pi]. Currents in Fig. 2 were recorded with extracellular solutions containing NMDG as the main cation and methanesulfonate (Fig. 2a–e) or citrate (Fig. 2f) as the main anion and low Cl^-, to reduce the number of potential permeant ions and to minimize conductance through native channels in HEK293 cells.

One advantage of the strong dependence of XPR1 activity on internal [Pi] is that in GUV recordings, only channels oriented with their cytoplasmic side facing the vesicle lumen should be activated under typical inside-out recording conditions where only the luminal side is exposed to high Pi. To test this hypothesis and confirm that XPR1 in GUVs is reconstituted in both orientations, we recorded from inside-out patches with intracellular (20 mM Pi) solution in the pipette and external (NMDG-methanesulfonate) solution in the bath. Under these conditions, outward XPR1 currents were recorded at positive voltages, exhibiting rectification consistent with channels oriented with the cytoplasmic side out. (Supplementary Fig. 6g). That our GUV data in Fig. 2 reproduces results from HEK cells therefore can be accounted for by the fact that we only applied high Pi on the luminal side.

To test whether the isolated protein is functional for Pi transport, we conducted proteoliposome flux assays and found that under the same buffer condition with citrate in which currents were observed by patch clamp recordings in Fig. 2f, liposomes reconstituted with hXPR1 protein, but not empty liposomes, showed time-dependent accumulation of [^{32}P] Pi. This transport was enhanced when the membrane potential was perturbed using a potassium gradient and the potassium ionophore valinomycin (Fig. 2k, l). These results could be accounted for by the voltage increasing the Pi driving force or hXPR1 open probability, consistent with the electrophysiological experiments. That is, since the external side of the vesicles was exposed to high (25 mM) Pi, only XPR1 with the cytoplasmic side facing out should have been activated, and the imposed voltage (negative on the external side relative to the lumen) should favor increased channel activity as well as increased driving force for Pi entry.

The putative ion permeation pathway

The ion channel-like conductance of hXPR1 observed by patch clamp recording elicited a closer examination of the TM domain of hXPR1 to identify potential ion permeation pathways. We found that each of the transmembrane segments TM1-4 is surrounded by the detergent environment individually and thus relatively isolated, suggesting that these four helices might not participate in ion translocation across the membrane. On the other hand, the TM5-10 are organized sequentially into a 6-helix bundle in a clockwise arrangement (viewed from the cytoplasmic side), forming a barrel-shaped structure. Aside from TM9, all helices within the barrel are oriented roughly perpendicular to the membrane surface. TM9, on the other hand, is tilted to ~45° with respect to the membrane. The protein's electrostatic surface reveals a highly positively charged vestibule at the center of the 6-helix bundle (Fig. 3a). This tunnel-like pathway is open to the cytoplasmic side and extends to the center of the protein. The positive surface of this vestibule arises from a series of positively charged residues, including Arg459, Arg466, Lys482, Arg570, Arg603, Arg604, and Arg611, and this overall positivity of the cavity is consistent with a pore that can conduct anions. To visualize the putative ion permeation pathway, we used the CAVER program[35]. The identified pore generally overlaps with the positive vestibule. The pore is accessible to solvent on the cytosolic side but is closed to the extracellular side in the apo-hXPR1 structure (Fig. 3b). The first ~one-third of the pore leading from the cytosolic entrance is formed by TM5a, 6, 7, 8, and 10. The tilted helix, TM9, meets the others in the middle, and all TM5-9 contribute to the central portion of the pore. The portion leading to the extracellular exit is closed by insertion of TM9 into the 6-helix barrel (Fig. 3b). The overall

https://doi.org/10.1038/s41467-025-59678-2

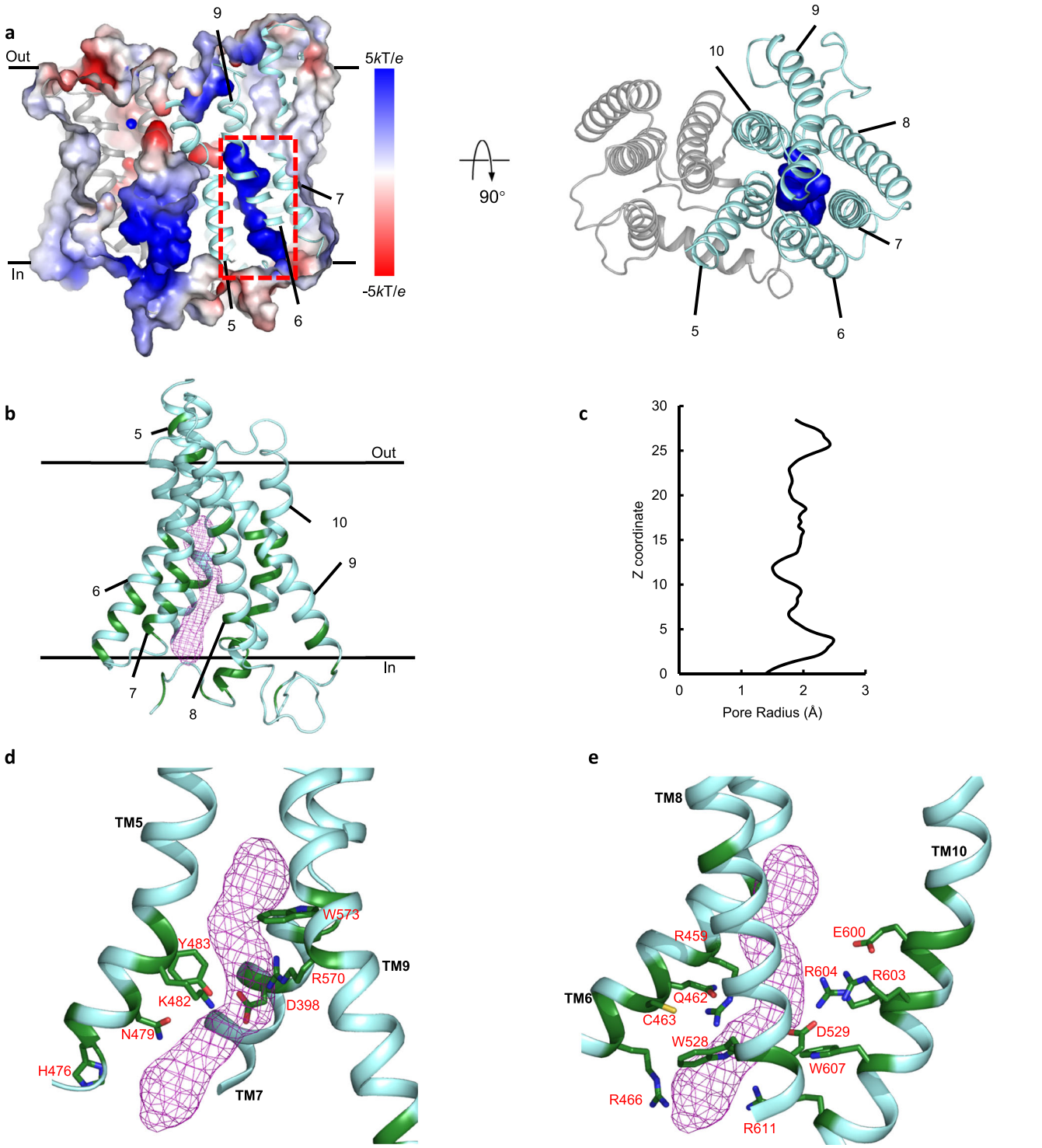

Fig. 3 | The putative pore of hXPR1. a (left) The solvent-accessible surface of the hXPR1 TMD colored by ±5 *kT*/*e* electrostatic potential calculated using APBS[62]. The secondary structures of TM1-4 are shown in gray and TM5-10 in light cyan. The positively charged vestibule formed at the center of the barrel-shaped helical bundle of TM5-10 is boxed in red. Two solid black lines indicate the membrane boundary. (right) The electrostatic surface–potential map depicts the same vestibule alone, viewed orthogonally from the extracellular space. **b** The putative pore location in hXPR1 inside the 6-helix barrel colored light cyan, and the pore pathway is depicted as a purple mesh. The residues on the TM5-10 that are conserved among hXPR1, atPHO1, and scSYG1 are colored in dark green. **c** Pore radius along the z coordinate. **d**, **e** Detailed view of the green-colored conserved pore-lining residues shown in stick model on TM5, 7, and 9 (**d**), and TM6, 8, and 10 (**e**).

diameter of the pore is around 4 Å, with a narrowest restriction of 3 Å. (Fig. 3c). Many of the surface-lining residues within this putative pore are conserved across different species among hXPR1, plant PHO1, and yeast SYG1 (Fig. 3d, e, Supplementary Fig. 7), suggesting this passage may be conserved among XPR1 homologs.

Structure of hXPR1 in the presence of Pi

To identify potential phosphate binding sites, we solved the structure of hXPR1 in buffer containing 25 mM sodium phosphate and 1 mM phytic acid ($InsP_6$), as inositol polyphosphates are known to facilitate Pi export upon binding to the SPX domain[28]. The soluble SPX domains

of Pi/$InsP_6$-hXPR1 map were poorly resolved compared to the TMD, as evident from the 2D classification analysis (Supplementary Fig. 3b), 3D reconstructions with either C1 or C2 symmetry imposed did not yield a structured and resolvable soluble domain. Thus, C2 symmetry was imposed for the final reconstruction of the Pi/$InsP_6$-hXPR1 map. The resolution of the resulting density map reached 2.3 Å, which is sufficient to recognize ions in the density (Supplementary Fig. 3, 4b, and Supplementary Movie 1). The overall TMD structure of Pi/$InsP_6$-hXPR1 does not differ significantly from that of apo-hXPR1, with an RMSD of only 0.271 Å. However, in the Pi/$InsP_6$-hXPR1 map, we identified a string of isolated, non-protein densities within the putative pore surrounded by TM5-10, that were not observed in the apo-hXPR1 map (Fig. 4a). It is highly likely that these densities represent locations for Pi ions as they travel through the pore. Based on these densities, we identified two locations along the putative pore which could serve as Pi coordination sites (Fig. 4b). The first site is situated near the narrowest restriction of the pore, where two positive charged residues Lys482 and Arg604 sandwich the putative Pi density, with side chains of other surrounding conserved residues Asp398, Tyr483, and Asp533 located more distally (Fig. 4c). The second site is near the extracellular end of the putative pore, in which the putative ion density is surrounded by three positive residues Arg604, which also participates in the first putative coordination site, in addition to Arg603 and Arg570 (Fig. 4d). These three positively charged core residues form a sequential arrangement with two consecutively on one helix and the other on an adjacent helix. Interestingly, this type of core interaction pattern is similar to the phosphate recognition region in triose-phosphate/phosphate translocator of plants, which also has three positively charged residues Lys204, Lys362, and Arg363 organized into a similar pattern (Supplementary Fig. 8)[36]. As such, these core residues may form a key Pi coordination site in the XPR1 putative pore. Located above the three arginine residues is Trp573, the aromatic residue whose side chain is positioned perpendicular to the pore. Although the string of densities extends beyond Trp573 (Fig. 4b), these extended densities are surrounded by non-conserved neutral residues.

Mutations of each of the three arginine residues (Arg570, Arg603, and Arg604) in the second putative Pi coordination site to alanine significantly impaired the Pi uptake in the flux assay (Fig. 4e). In addition, in patch clamp assays, while large currents could be recorded from R570A in 10 mM Pi with methanesulfonate as the main anion, currents were greatly reduced in 75 mM Pi (Fig. 4f), an effect opposite to that observed with WT XPR1 (Fig. 2g). This suggests the mutation selectively reduces Pi permeability, consistent with a role of R570 in Pi coordination.

The positions of residues lining the surface of the putative pore have little difference between the apo-hXPR1 and Pi/$InsP_6$-hXPR1 maps, as evident from a TM5-10 RMSD of 0.267 Å between the two structures. Thus, the dimension of this pore in the Pi/$InsP_6$-hXPR1 structure is very similar to that of apo-hXPR1, with the narrowest diameter of 3 Å. In addition, in both structures, the TM9 forms a single continuous transmembrane helix, with the top segment inserted directly into the pore, effectively blocking the exit towards the extracellular space. Thus, we propose that both structures represent the closed state of hXPR1. Consistent with a failure of $InsP_6$ to open the channel, we observed no appreciable effect of 1 mM $InsP_6$ on XPR1 current or Pi flux (Supplementary Figs. 12b, c).

The C-terminal tail bridges the SPX domain and the TMD

In the cytosolic helical bundle of one of the protomers of the apo-hXPR1, we identified a short α-helix that does not map to the SPX domain. The density map of this protomer displays a well-resolved connection between this short cytoplasmic helix and the end of TM10, the last TM helix of TMD (Supplementary Fig. 9a). This connection allows us to build a portion of this protomer's C-terminal cytoplasmic tail. This short helix, which we denote as intracellular loop 4 (IL4), was assigned to residues 636–646 (Supplementary Fig. 9b) linked directly to TM10 via a loop. Given the different orientations of SPX domains with respect to the TMD between two protomers in the apo structure (Supplementary Fig. 9c) and the unresolvability of SPX in the Pi/$InsP_6$ structure, we hypothesize that the SPX domain is flexible and might undergo conformational changes in response to different conditions. The C-terminal cytoplasmic tail, with one end connecting directly to TMD and the other forming a short helix that bundles with the SPX domain, potentially serves to bridge between the SPX domain and TMD and provides the architectural basis for the allosteric regulation of the SPX domain on TMD.

Discussion

In this study, we investigated the structure-function relationship of human XPR1. Our structures revealed that hXPR1 is dissimilar to known transporters but has features consistent with ion channel function: TM5-10 form a helical barrel, and within this barrel a central cavity is identified which reveals a partial pathway with appropriate diameter and charge to conduct anions; the additional densities seen coordinated to positively charged side chains within that pathway in the presence of Pi likely represent Pi coordination sites.

Electrophysiological recordings from hXPR1 in excised patches revealed large unitary currents with a linear open channel I-V relation in HEK293 cells, and large macroscopic inward currents in GUVs, including in the absence of Pi or with Pi as the sole internal anion, all supporting the conclusion that XPR1 can function as an ion channel that is permeable to Pi and relatively non-selective for anions. The Pi transport activity was further confirmed using proteoliposomal flux assays. The lack of structural similarity between XPR1 and known transporters, together with the identification of channel-like structural topology including a pore architecture with putative Pi binding sites, supports that XPR1 transports Pi as a channel rather than as a Pi transporter with uncoupled ion channel activity, a hypothesis further supported by observations that mutations of the key arginine residues within one of the putative Pi coordination sites impaired Pi uptake in the flux assay, and one of them showed reduced Pi permeability in patch clamp recordings.

The rate of Pi transport (~10 Pi per XPR1 s^{-1}, from the 1 min time point) is orders of magnitude less than the charge movement through the open channel measured with patch clamp at −50 mV (Fig. 2f), owing to several factors that cannot all be quantified. First, in the flux assay, the initial rate is likely to be underestimated owing to the time resolution of the measurement. Second, the membrane voltage is not controlled and is likely to favor a low Po (<0.1) if V is near 0 based on the V-dependence of activation (Fig. 2d). Third, the fraction of XPR1 protein molecules that are functional in the flux assay and have correct membrane orientation to be activated by high external Pi is unknown. Finally, in the patch clamp assay, Pi flux represents only a fraction of the total charge movement as the channel is not selective for Pi over the predominant anion, methanesulfonate.

Strong inward rectification and large unitary conductance clearly distinguished XPR1 activity from native channels occasionally observed in HEK293 cells. The inward rectification arises from voltage-dependent activation of the channel at negative voltages. Activation is also Pi-dependent, with little activity in the absence of Pi and shifts in the G-V relation to more positive voltages as $[Pi]_i$ is increased. The channel appears to attain a high open probability, near unity, at maximally effective voltages in high $[Pi]_i$, as unitary currents activated at −100 mV in 20 mM Pi during voltage ramps exhibit no sign of transient closure (Fig. 2e), and the maximal macroscopic conductance at 10 or 75 mM Pi is constant (Fig. 2j).

The mechanistic basis of voltage-dependent activity is unknown but is unlikely to simply reflect voltage-dependent block of the pore by impermeant ions, given the slow activation kinetics that required up to 0.5 s to reach equilibrium (Fig. 2b). Alternative possibilities include

https://doi.org/10.1038/s41467-025-59678-2

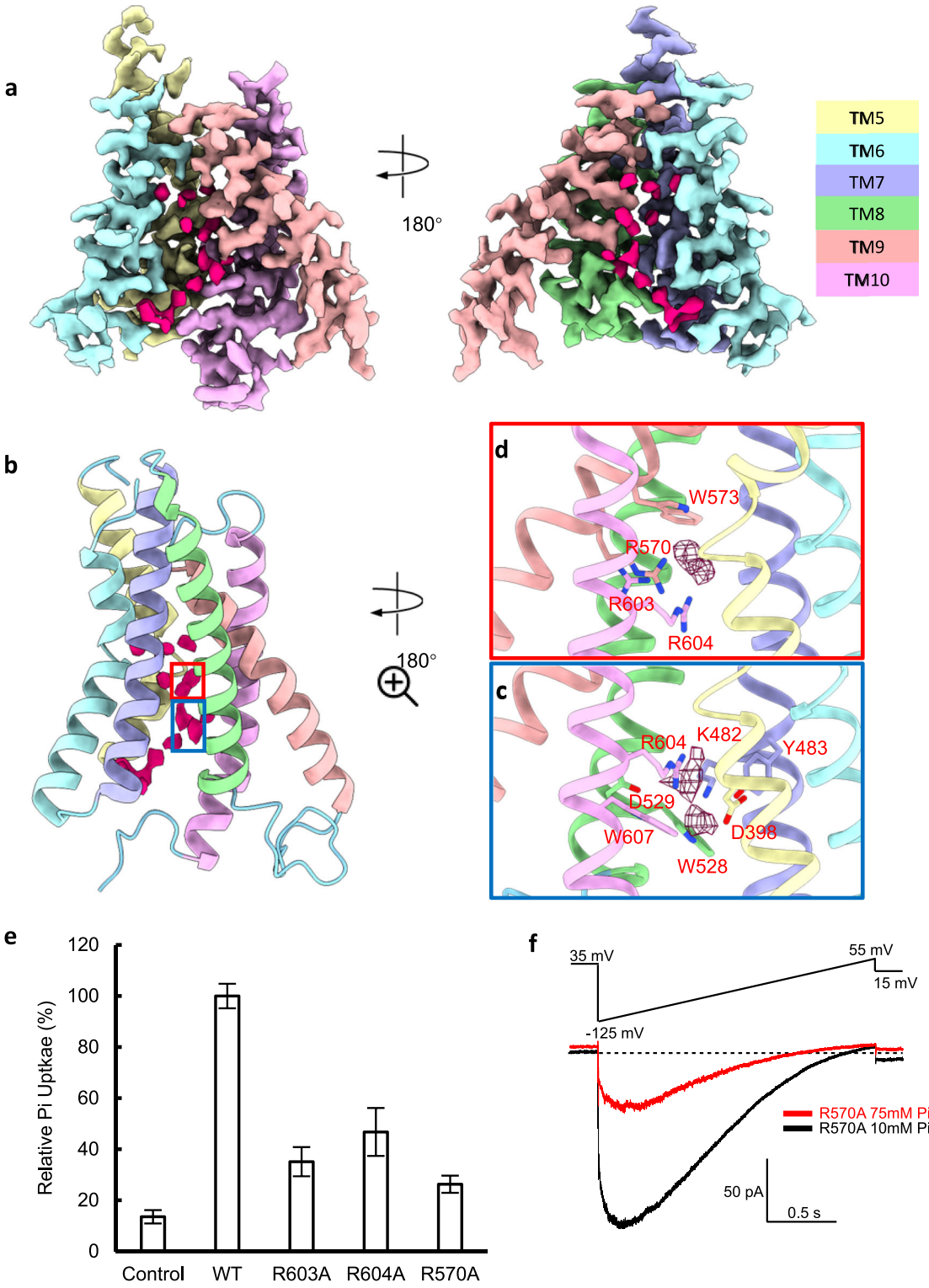

Fig. 4 | Putative ion coordination sites. a The density map of TM5-10 of Pi/InsP$_6$-hXPR1, with each TM helix colored individually at a contour level of 10.96σ. The non-protein isolated densities within the pore are colored in pink red. Densities from TM5 and TM10 (right), or TM7 and TM8 (left), are removed to expose the pore. **b** The string of putative ion densities in gray depicted at a 10.96σ contour level with the cartoon representation of Pi/InsP$_6$-hXPR1 TM5-10 structure. Densities corresponding to the two putative ion coordination sites are boxed in red and blue. **c**, **d** Close-up views of the two putative ion coordination sites indicated in the colored boxes in (**b**), with the ion density shown at a 5.35σ contour level. **e** Relative Pi transport of the alanine mutations of three arginine residues within the red-colored putative Pi binding in (**c**). The relative transport was measured at the 20-min time point with the addition of valinomycin. Means ± SEM plotted ($n = 4$ independent assays). **f** XPR1 R570A currents evoked from a GUV patch by voltage ramps are decreased as internal Pi is increased from 10 mM (black) to 75 mM (red), using 10 Cl K-MSA internal solutions with external **0** Pi, 10 NMDG-Cl. Each curve represents the average of 5 traces (as in Fig. 2g).

voltage-dependent conformational changes in the protein (i.e., a voltage-sensor domain), or a dependence of channel opening or closing on voltage-dependent binding of a permeant ion to a site or sites within the pore, a mechanism which has been proposed by various groups to contribute to the voltage-dependent activation of CLC_0 chloride channels[37]. That the apparent gating charge of XPR1 activation ($z = -1.8$ e, Fig. 2d) is identical to the average charge of Pi at pH 7.4 and activation is shifted to more positive voltages as internal [Pi] is increased is consistent with the notion that Pi binding in the pore may contribute to the voltage-dependence of activation. This hypothesis may also explain why a recent study[38] reported that XPR1 conductance is voltage-independent (i.e., has a linear macroscopic I-V relation), as they used internal and external solutions that both contain 100 mM Pi. Likewise, the use of high Pi might explain why this group reported an increase in XPR1 conductance by 1 mM $InsP_6$, although we saw no appreciable effect of $InsP_6$ at this concentration on current or Pi flux under our assay conditions.

With our structures, we could map the locations of PFBC mutations (Supplementary Fig. 11a). Many of the mutations were known to be located on the SPX domain, which could potentially disrupt the SPX regulation of the Pi export activity. On the other hand, our structures provide novel perspectives on how mutations in other parts of hXPR1 could lead to diseases. Three mutations are located within the TM5-10 helical barrel forming the putative ion permeation pore: Arg459, Arg570, and Ile575 (Supplementary Fig. 11b). Specifically, mutations of Arg459 and Arg570 have been shown to lead to reduced Pi export without affecting the protein expression levels[5,15]. These two arginine residues are conserved (Supplementary Fig. 7), with Arg459 located near the narrowest constraint and Arg570 within the putative Pi coordination site (Figs. 3e and 4c), in support of the hypothesis that Pi permeates through the putative pore. Moreover, both our flux assay and electrophysiological recordings showed that the mutation of R570A impaired Pi transport, which supports its role in the putative Pi coordination site and may help explain the pathological mechanism of the PFBC-causing variant R570L.

In addition, three disease-associated mutation sites, Asn619, Arg624, and Ile629, are located within the C-terminal cytoplasmic tail on the loop connecting TM10 to IL4 (Supplementary Figs. 10, 11b). Asn619 and Arg624 are also conserved across XPR1 homologs (Supplementary Fig. 7), and these mutations were documented to reduce XPR1-mediated Pi efflux as well[5]. Combined with the potential flexibility of the SPX domain, these results suggest a novel role for the C-terminal cytoplasmic tail in bridging the SPX domain with the TMD to achieve allosteric regulation. Indeed, it has been hypothesized that part of the C-terminal tail could serve as the plug that restricts the entrance into the pore[39–41], and the binding of $InsP_8$ could alter the SPX conformation to rearrange the structure of the C-terminal tail and lessen its restriction of the pore[40,41].

Both our structures likely represent a closed state based on the pore size and the TM9 blockade towards the extracellular side. It is possible that an alternative, perhaps transient, state not observed in our data, allows Pi exit to the extracellular side. It is still unclear how the pore would open. To explore reasonable alternative structures, we used Alphafold2 to predict structures for the transmembrane domain[42]. When compared, the helix arrangements in our experimental structures and the most probable prediction are quite similar, with one major difference focusing on TM9. AlphaFold2 predicts that TM9 is broken into two segments with a kink in the middle, and the segment closer to the extracellular space is rotated away from the 6-helix bundle (Supplementary Fig. 10a). In this conformation, TM9 no longer blocks the ion permeation pathway, and the pore is open to both sides of the membrane (Supplementary Fig. 10b). Trp573 resides next to the kink, and in our closed structure the side chain of Trp573 is situated directly above the putative Pi binding site, with Arg570 being one helical turn away (Supplementary Fig. 10a). Thus, we propose the hypothesis that a bent conformation of TM9 at Trp573 may open hXPR1 to allow Pi efflux. In Pi transporter SLC20, a kink is observed in a helix lining the Pi binding pocket at a conserved tryptophan residue, and the helix-bending mechanism was proposed to control the opening and closing of the gate that allows the Pi release[43]. Thus, we propose the hypothesis that a bent conformation of TM9 at Trp573 may open hXPR1 to allow Pi efflux. After the submission of this manuscript, two groups reported cryo-EM studies of XPR1, with both describing lower-resolution structures of XPR1 in which the TM9 is kinked similarly to the aforementioned AlphaFold prediction[38,39]. These results support our hypothesis of an open XPR1 conformation that entails a continuous tunnel allowing the observed ion channel activity. However, the exact mechanism by which the bent conformation of TM9 is triggered and whether it is coupled to the binding of inositol polyphosphate species or to additional undiscovered factors requires further studies.

In summary, our structural and functional data established that hXPR1 transports Pi as an ion channel whose activity is regulated by intracellular Pi concentration and membrane voltage. It is likely that if XPR1 functions as a non-selective anion channel in cells, its activity must be tightly regulated. The requirement that XPR1 activates only at negative voltages with high intracellular Pi assures that the channel will only be open under conditions where the electrochemical gradient favors Pi efflux. In addition, the Pi export activity of XPR1 in cells is thought to be critically dependent upon the presence of higher-order intracellular inositol pyrophosphates such as InsP7 and InsP8[27–29], which are only transiently generated as a result of excess Pi conditions[44–46]. Additional means of regulating XPR1 activity have also been reported[10,19,47]. These regulatory mechanisms may allow the channel to act as an "escape valve" for Pi that is only transiently activated, and this pattern of Pi efflux could potentially be linked to the phenomena of rapid Pi release documented in various cell types[48,49], specifically in pancreatic β-cells in which XPR1 was established to mediate the "phosphate flush"[50]. Our results provide insights into XPR1's role in maintaining intracellular Pi homeostasis and reveal the structural and functional impacts of mutations causing PFBC, enabling further investigations into their mechanisms and approaches to therapeutics.

Methods

Expression and purification of hXPR1

The cDNA of human XPR1 (Uniprot: Q9UBH6) was synthesized with a Strep-tag II peptide fused at the C-terminus, and cloned into the pBacMam vector for expression in HEK293S GnTI$^-$ cells[51].

The purification was carried out at 4 °C. The cell pellet from 2 L of HEK293S GnTI culture was resuspended in 100 mL lysis buffer containing 20 mM Tris, 150 mM NaCl, and 2 mM $MgCl_2$ buffered at pH 7.4, supplemented with 1 protease inhibitor cocktail tablet (Roche) and 5 µL of nuclease (Thermo Fisher) per 50 mL buffer. The cells were directly solubilized by adding 1.5% (w/v) n-dodecyl-β-D-maltoside (DDM, Anatrace) and 0.15% (w/v) cholesteryl hemisuccinate (CHS, Anatrace) for two hours and were centrifuged at 180,000 × *g* for 1 h. The supernatant containing detergent-solubilized hXPR1 protein was loaded onto Strep-Tactin HP affinity purification column (Cytiva) and washed with wash buffer containing 20 mM Tris pH 7.4, 150 mM NaCl, 0.005% (w/v) glycodiosgenin (GDN, Anatrace), 0.005% (w/v) lauryl maltose neopentyl glycol (LMNG, Anatrace), and 0.0001% CHS. hXPR1 protein was then eluted with wash buffer supplemented with 5 mM desthiobiotin (Sigma Aldrich). The eluted protein was concentrated using a centrifugal filter unit with a 50 kDa cut-off down (Milipore) to 500 µL volume.

For apo-hXPR1 structural studies, the concentrated protein was loaded onto Superose 6 10/300 GL size-exclusion column (Cytiva) pre-equilibrated with wash buffer. For hXPR1 in the presence of Pi/InsP6, the size-exclusion column was pre-equilibrated using 25 mM sodium phosphate, 150 mM NaCl, and 1 mM phytic acid ($InsP_6$) at pH 7.4 with the same GDN/LMNG/CHS detergent mixture concentration.

Size Exclusion Chromatography-Multi-Angle Light Scattering (SEC-MALS)

Data were collected using a Dawn Ambient light scattering instrument equipped with a 661 nm laser (Wyatt). The whole system is linked to an HPLC system with UV absorbance detection at 280 nm (Agilent) and an Optilab (Wyatt) for differential refractive index (dRI) measurements. Approximately 100 µg of purified hXPR1 protein was injected and flowed through a Superose 6 10/300 GL column (Cytiva) equilibrated with 20 mM Tris pH 7.4, 150 mM NaCl, 0.005% (w/v) GDN, 0.005% (w/v) LMNG, and 0.0001% CHS. Data was analyzed using the Astra software (Wyatt). A d*n*/d*c* of 0.185 is used for the detergent mixture, and ε is set to 1.64 ml/mg.cm.

Cryo-EM sample preparation and data collection

hXPR1 samples in different conditions were concentrated to 10–20 mg/mL for cryo-EM grid preparation. Cryo grids were prepared using the Thermo Fisher Vitrobot Mark IV, maintained at 8 °C and 100% relative humidity. Quantifoil R1.2/1.3 Cu 300 mesh grids were glow-discharged in air for 15 s using Pelco Easyglow. 3.5 µL hXPR1 sample was applied to each glow-discharged grid. After blotting with filter paper (Ted Pella, Prod. 47000-100) for 3.5–4.5 s, the grids were plunged into liquid ethane cooled with liquid nitrogen.

Cryo-EM data were collected using Thermo Fisher Titan Krios microscope at 300 kV with a Quantum energy filter (Gatan) with 15 eV slit width, and a K3 Summit direct electron detector (Gatan). Movie stacks were collected in super-resolution mode with defocus values ranging between −2.2 µm and −0.8 µm at 105,000× nominal magnification (calibrated per pixel size of 0.416 Å in super-resolution). The exposure time for each stack was 2.6 s, fractionated into 40 frames, with a total accumulated dose of 50e^-/Å^2. A total of 16,297 movies were collected for the apo-hXPR1 dataset, and 15,802 movies for the Pi/InsP_6-hXPR1 dataset.

Cryo-EM data processing

For apo-hXPR1, the movie stacks were motion-corrected with MotionCor2[52] and the aligned final images were binned (2 × 2) to 0.832 Å per pixel size. Dose weighting was performed during motion correction, and the defocus values were estimated with CTFFIND4[53]. After manual curation, a total of 14,168 micrographs were selected, which had a CTF-fitted resolution value below 4 Å. A total of 8,468,502 particles were automatically picked using templates from preliminary analysis and extracted for 2D classifications in cryoSPARC[54]. 813,777 particles were selected from the good 2D classes for ab initio 3D reconstruction and imported into Relion4.0 for 3D classification[55]. Two good classes with recognizable structural features containing 230,861 particles were selected and imported back to cryoSPARC for non-uniform refinement using C1 symmetry with CTF refinement[56], which yielded a map with an overall resolution of 3.4 Å. Resolutions were estimated using the gold-standard Fourier shell correlation with a 0.143 cut-off. Local resolution was estimated using ResMap[57].

The data processing for Pi/InsP6-hXPR1 followed a similar workflow. A total of 14,603 micrographs were selected, which had a CTF-fitted resolution value below 4 Å after motion correction and CTF estimation. 11,247,130 particles were automatically picked, with 2,428,881 particles selected from the good 2D classes. A final set containing 536,955 particles was selected after 3D classifications and used for non-uniform refinement using C2 symmetry with CTF refinement, which yielded a map with an overall resolution of 2.3 Å.

Model building and refinement

The transmembrane domain of apo-hXPR1 was built using the AlphaFold prediction[42] as the initial model. Carbon backbones and the side chains were adjusted based on the density map. The SPX domain of apo-hXPR1 was built using the solved crystal structure[26] (PDB: 5IJH) as a template to perform rigid body docking into the density maps and modified with flexible fitting. The model of Pi/InsP6-hXPR1 was built using the apo-hXRP1 as the initial reference and adjusted based on the density map. Model building was conducted in Coot[58]. Structural refinements were carried out in PHENIX[59] in real space with secondary structure and geometry restraints. The channel was calculated using CAVER 3.0.3[35] with a minimum probe radius of 1.2, shell depth of 3, shell radius of 2, and clustering threshold of 3.5.

Proteoliposome preparation

For proteoliposomes used in Pi transport assay, brain polar lipid extract (Avanti) was mixed with 3% (w/w) cholesterol (Avanti) in chloroform, dried under argon gas stream, and further dried overnight in vacuum. Lipids were then hydrated at 10 mg/mL with assay buffer containing 140 mM N-Methyl-D-glucamine (NMDG, Sigma Aldrich), 20 mM HEPES, 1 mM phosphoric acid, 10 mM hydrochloric acid, adjusted to pH 7.4 with citric acid. The lipids were flash frozen in liquid nitrogen, thawed for a total of five freeze-thaw cycles, and then extruded 21 times using polycarbonate filters with a pore size of 50 nm (Whatman) to obtain unilamellar vesicles. 0.01% of DDM was added to destabilize the lipid, and then purified wild-type or mutant hXPR1 proteins in 0.03% DDM were added with a 1:500 (w/w) protein-to-lipid ratio. The mixture was incubated for 1 h, and detergent was removed by the addition of Bio-Beads SM-2 (Bio-Rad). Collected liposomes were flash frozen and stored at −80 °C until further use.

Giant unilamellar vesicles (GUVs) used in patch clamp were made from 20 µL brain polar lipid extract with 10% (w/w) cholesterol in chloroform at 5 mg/mL by electroformation using the Vesicle Prep Pro (Nanion Technologies) in 250 µL buffer containing 2 mM HEPES at pH 7.4, 1 mM EGTA, 400 mM sorbitol. Purified hXPR1 protein in 0.03% DDM at 0.1 mg/mL was mixed with GUV solution and diluted to a final concentration of approximately 50–500 ng/mL (~1:90,000 to ~1:900,000 protein-to-lipid molar ratio) and incubated overnight at 4 °C with SM-2 Bio-Beads (Bio-Rad).

Electrophysiology

Ionic currents were recorded using the patch clamp technique in the inside-out or whole cell configuration. Data were acquired and analyzed as previously described[60]. Traces shown in the figures are digitally filtered at 5 kHz. Voltages have been corrected for liquid junction potentials, calculated according to the stationary Nernst–Planck equation using LJPcalc[61]. The bath was grounded through an agar bridge. All experiments were performed at room temperature (22–24 °C). External solutions contained in mM: **NMDG-MSA** −140 N-methyl-D-glucamine (NMDG), 20 HEPES, 5 EGTA, 10 HCl, with or without 1 Pi added as phosphoric acid and adjusted to pH 7.2 with 112 methanesulfonic acid (MSA). **NMDG-citrate** −140 NMDG, 20 HEPES, 1 phosphoric acid, 10 HCl, adjusted to pH 7.2 with 17.4 citric acid. **NMDG-Cl** − 10 NMDG, 20 HEPES, 260 Sucrose, pH 7.2 with 8.72 HCl. Internal solutions contained in mM: **20 Pi, 0.07 Ca, K-MSA** − 110 KOH, 10 K_2HPO_4, 10 KH_2PO_4, 0.42 HCl, 4.79 $CaCl_2$,5 HEDTA, pH to 7.2 with 92.5 MSA, and free Ca^{2+} = 66.0 ± 5.9 µM measured by Ca^{2+} electrode (Orion Research). **0 Pi, 10 Cl, K-MSA** − 140 KOH, 20 HEPES, 5 EGTA, 10 HCl, pH 7.2 with 115.1 MSA. **75 Pi, 10 Cl, K-MSA** − 54 K2HPO4, 21 KH2PO4, 20 HEPES, 5 EGTA, 10 KCl, pH 7.2 with 16 KOH. **10 Pi, 0 Ca, K-MSA** - as a 13:2 mixture of 0 and 75 Pi, 10 Cl K-MSA. **75 Pi, 0 Cl, K-MSA** − 54 K2HPO4, 21 KH2PO4, 20 HEPES, 5 EGTA, pH 7.2 with 16 KOH.

Proteoliposomal Pi uptake assay

Pi uptake activity was measured with reconstituted proteoliposomes containing either wild-type or mutant hXPR1. The control was empty liposomes. To generate a potassium gradient used to perturb the membrane potential, thawed liposomes in assay buffer containing 140 mM NMDG, 20 mM HEPES, 1 mM phosphoric acid, 10 mM hydrochloric acid adjusted to pH 7.2 with citric acid, were added with 60 mM NaCl and 5 mM KCl. The

mixture underwent an additional five freeze-thaw cycles using liquid nitrogen. The liposomes were extruded again using a 200 nm filter membrane for homogeneity, yielding sealed XPR1-containing liposomes with 5 mM internal KCl. The extruded liposomes were exchanged into assay buffer containing 60 mM KCl and 5 mM NaCl using a PD-10 desalting column (Cytiva). A total volume of 5 µl of liposomes was added to a 50-µl reaction solution. Carrier non-radioactive sodium phosphate (1 M stock, pH 7.4) was added at a final concentration of 25 mM, along with 0.1 mCi/mL [^{32}P] orthophosphate (5 µCi total, diluted from stock of 8500–9120 Ci/mmole; carrier-free, PerkinElmer) to initiate the reaction. For experiments in which the membrane potential was perturbed, 200 nM valinomycin was added to the reaction mixture. The mixture was incubated for various time points at 37 °C. The reaction was rapidly filtered with a G-25 spin column (Cytiva) to remove unincorporated Pi. Radioactivity was determined by liquid scintillation counting.

Reporting summary

Further information on research design is available in the Nature Portfolio Reporting Summary linked to this article.

Data availability

The atomic coordinates have been deposited in the Protein Data Bank with the accession codes 9CKZ (hXPR1 in apo state (ligand-free)) and 9CL0 (hXPR1 in the presence of inorganic phosphate and phytic acid). The cryo-EM density maps have been deposited in the Electron Microscopy Data Bank (EMDB) with the accession codes EMD-45656 (hXPR1 in apo state (ligand-free)) and EMD-45657 (hXPR1 in the presence of inorganic phosphate and phytic acid). All electrophysiological data needed to evaluate the conclusions in the paper are present in the paper, and the raw data are available upon request. Source data are provided with this paper.

References

1. Tailor, C. S., Nouri, A., Lee, C. G., Kozak, C. & Kabat, D. Cloning and characterization of a cell surface receptor for xenotropic and polytropic murine leukemia viruses. *Proc. Natl Acad. Sci. USA* **96**, 927–932 (1999).
2. Yang, Y. L. et al. Receptors for polytropic and xenotropic mouse leukaemia viruses encoded by a single gene at Rmc1. *Nat. Genet.* **21**, 216–219 (1999).
3. Giovannini, D., Touhami, J., Charnet, P., Sitbon, M. & Battini, J.-L. Inorganic phosphate export by the retrovirus receptor XPR1 in metazoans. *Cell Rep.* **3**, 1866–1873 (2013).
4. Legati, A. et al. Mutations in XPR1 cause primary familial brain calcification associated with altered phosphate export. *Nat. Genet.* **47**, 579–581 (2015).
5. López-Sánchez, U. et al. Characterization of XPR1/SLC53A1 variants located outside of the SPX domain in patients with primary familial brain calcification. *Sci. Rep.* **9**, 6776 (2019).
6. Poirier, Y., Thoma, S., Somerville, C. & Schiefelbein, J. Mutant of Arabidopsis deficient in xylem loading of phosphate. *Plant Physiol.* **97**, 1087–1093 (1991).
7. Stefanovic, A. et al. Over-expression of PHO1 in Arabidopsis leaves reveals its role in mediating phosphate efflux. *Plant J.* **66**, 689–699 (2011).
8. Arpat, A. B. et al. Functional expression of PHO1 to the Golgi and trans-Golgi network and its role in export of inorganic phosphate. *Plant J. Cell Mol. Biol.* **71**, 479–491 (2012).
9. Ma, B. et al. A plasma membrane transporter coordinates phosphate reallocation and grain filling in cereals. *Nat. Genet.* **53**, 906–915 (2021).
10. Xu, C. et al. A phosphate-sensing organelle regulates phosphate and tissue homeostasis. *Nature* **617**, 798–806 (2023).
11. Takado, M. et al. Phosphate uptake restriction, phosphate export, and polyphosphate synthesis contribute synergistically to cellular proliferation and survival. *J. Biol. Chem.* **299**, 105454 (2023).
12. Jennings, M. L. Role of transporters in regulating mammalian intracellular inorganic phosphate. *Front. Pharmacol.* **14**, 1163442 (2023).
13. Anheim, M. et al. XPR1 mutations are a rare cause of primary familial brain calcification. *J. Neurol.* **263**, 1559–1564 (2016).
14. Tang, L.-O. et al. Biallelic XPR1 mutation associated with primary familial brain calcification presenting as paroxysmal kinesigenic dyskinesia with infantile convulsions. *Brain Dev.* **43**, 331–336 (2021).
15. Guo, X.-X. et al. Spectrum of SLC20A2, PDGFRB, PDGFB, and XPR1 mutations in a large cohort of patients with primary familial brain calcification. *Hum. Mutat.* **40**, 392–403 (2019).
16. Orimo, K. et al. A Japanese family with idiopathic basal ganglia calcification carrying a novel XPR1 variant. *J. Neurol. Sci.* **451**, 120732 (2023).
17. Yoon, S., Chung, S. J. & Kim, Y. J. Primary familial brain calcification with XPR1 mutation presenting with cognitive dysfunction. *J. Clin. Neurol.* **20**, 229–231 (2024).
18. Lemos, R. R. et al. Update and mutational analysis of SLC20A2: a major cause of primary familial brain calcification. *Hum. Mutat.* **36**, 489–495 (2015).
19. Bondeson, D. P. et al. Phosphate dysregulation via the XPR1:KIDINS220 protein complex is a therapeutic vulnerability in ovarian cancer. *Nat. Cancer* **3**, 681–695 (2022).
20. Chen, W. et al. Xenotropic and polytropic retrovirus receptor 1 (XPR1) promotes progression of tongue squamous cell carcinoma (TSCC) via activation of NF-κB signaling. *J. Exp. Clin. Cancer Res.* **38**, 167 (2019).
21. Akasu-Nagayoshi, Y. et al. PHOSPHATE exporter XPR1/SLC53A1 is required for the tumorigenicity of epithelial ovarian cancer. *Cancer Sci.* **113**, 2034–2043 (2022).
22. Mao, X., Guo, S., Gao, L. & Li, G. Circ-XPR1 promotes osteosarcoma proliferation through regulating the miR-214-5p/DDX5 axis. *Hum. Cell* **34**, 122–131 (2021).
23. Wu, W., Zhang, Y., Li, X., Wang, X. & Yuan, Y. miR-375 inhibits the proliferation, migration and invasion of esophageal squamous cell carcinoma by targeting XPR1. *Curr. Gene Ther.* **21**, 290–298 (2021).
24. Hu, J. et al. CircGNB1 facilitates the malignant phenotype of GSCs by regulating miR-515-5p/miR-582-3p-XPR1 axis. *Cancer Cell Int.* **23**, 132 (2023).
25. Hu, Y. et al. The miR-4732-5p/XPR1 axis suppresses the invasion, metastasis, and epithelial-mesenchymal transition of lung adenocarcinoma via the PI3K/Akt/GSK3β/Snail pathway. *Mol. Omics* **18**, 417–429 (2022).
26. Wild, R. et al. Control of eukaryotic phosphate homeostasis by inositol polyphosphate sensor domains. *Science* **352**, 986–990 (2016).
27. Wilson, M. S., Jessen, H. J. & Saiardi, A. The inositol hexakisphosphate kinases IP6K1 and −2 regulate human cellular phosphate homeostasis, including XPR1-mediated phosphate export. *J. Biol. Chem.* **294**, 11597–11608 (2019).
28. López-Sánchez, U. et al. Interplay between primary familial brain calcification-associated SLC20A2 and XPR1 phosphate transporters requires inositol polyphosphates for control of cellular phosphate homeostasis. *J. Biol. Chem.* **295**, 9366–9378 (2020).
29. Li, X. et al. Control of XPR1-dependent cellular phosphate efflux by InsP8 is an exemplar for functionally-exclusive inositol pyrophosphate signaling. *Proc. Natl Acad. Sci. USA* **117**, 3568–3574 (2020).
30. Wege, S. et al. The EXS domain of PHO1 participates in the response of shoots to phosphate deficiency via a root-to-shoot signal. *Plant Physiol.* **170**, 385–400 (2016).
31. Xie, T. et al. Rational exploration of fold atlas for human solute carrier proteins. *Structure* **30**, 1321–1330.e5 (2022).

32. Holm, L. Dali server: structural unification of protein families. *Nucleic Acids Res.* **50**, W210–W215 (2022).
33. Boudker, O. & Verdon, G. Structural perspectives on secondary active transporters. *Trends Pharmacol. Sci.* **31**, 418–426 (2010).
34. Hosaka, T. et al. Structural mechanism for light-driven transport by a new type of chloride ion pump, Nonlabens marinus Rhodopsin-3 *◆. *J. Biol. Chem.* **291**, 17488–17495 (2016).
35. Chovancova, E. et al. CAVER 3.0: a tool for the analysis of transport pathways in dynamic protein structures. *PLoS Comput. Biol.* **8**, e1002708 (2012).
36. Lee, Y. et al. Structure of the triose-phosphate/phosphate translocator reveals the basis of substrate specificity. *Nat. Plants* **3**, 825–832 (2017).
37. Jentsch, T. J. & Pusch, M. CLC chloride channels and transporters: structure, function, physiology, and disease. *Physiol. Rev.* **98**, 1493–1590 (2018).
38. Lu, Y. et al. Structural basis for inositol pyrophosphate gating of the phosphate channel XPR1. *Science* **386**, eadp3252 (2024). 0.
39. Yan, R. et al. Human XPR1 structures reveal phosphate export mechanism. *Nature* **633**, 960–967 (2024).
40. Zhu, Q. et al. Transport and InsP8 gating mechanisms of the human inorganic phosphate exporter XPR1. *Nat. Commun.* **16**, 2770 (2025).
41. Wang, X. et al. KIDINS220 and InsP8 safeguard the stepwise regulation of phosphate exporter XPR1. Preprint at *bioRxiv* https://doi.org/10.1101/2025.01.17.633679 (2025).
42. Jumper, J. et al. Highly accurate protein structure prediction with AlphaFold. *Nature* **596**, 583–589 (2021).
43. Tsai, J.-Y. et al. Structure of the sodium-dependent phosphate transporter reveals insights into human solute carrier SLC20. *Sci. Adv.* **6**, eabb4024 (2020).
44. Nagpal, L., He, S., Rao, F. & Snyder, S. H. Inositol pyrophosphates as versatile metabolic messengers. *Annu. Rev. Biochem.* **93**, 317–338 (2024).
45. Saiardi, A. How inositol pyrophosphates control cellular phosphate homeostasis? *Adv. Biol. Regul.* **52**, 351–359 (2012).
46. Khan, A., Mallick, M., Ladke, J. S. & Bhandari, R. The ring rules the chain - inositol pyrophosphates and the regulation of inorganic polyphosphate. *Biochem. Soc. Trans.* **52**, 567–580 (2024).
47. Vetal, P. V. & Poirier, Y. The Arabidopsis PHOSPHATE 1 exporter undergoes constitutive internalization via clathrin-mediated endocytosis. *Plant J. Cell Mol. Biol.* **116**, 1477–1491 (2023).
48. Abood, L. G., Koketsu, K. & Koyama, I. Outflux of inorganic and organic phosphate during membrane depolarization of excitable tissues. *Nature* **191**, 395–396 (1961).
49. Freinkel, N., El Younsi, C., Bonnar, J. & Dawson, R. M. C. Rapid transient efflux of phosphate ions from pancreatic islets as an early action of insulin secretagogues. *J. Clin. Invest.* **54**, 1179–1189 (1974).
50. Barker, C. J. et al. XPR1 mediates the pancreatic β-cell phosphate flush. *Diabetes* **70**, 111–118 (2021).
51. Goehring, A. et al. Screening and large-scale expression of membrane proteins in mammalian cells for structural studies. *Nat. Protoc.* **9**, 2574–2585 (2014).
52. Zheng, S. Q. et al. MotionCor2: anisotropic correction of beam-induced motion for improved cryo-electron microscopy. *Nat. Methods* **14**, 331–332 (2017).
53. Rohou, A. & Grigorieff, N. CTFFIND4: fast and accurate defocus estimation from electron micrographs. *J. Struct. Biol.* **192**, 216–221 (2015).
54. Punjani, A., Rubinstein, J. L., Fleet, D. J. & Brubaker, M. A. cryoSPARC: algorithms for rapid unsupervised cryo-EM structure determination. *Nat. Methods* **14**, 290–296 (2017).
55. Scheres, S. H. W. RELION: implementation of a Bayesian approach to cryo-EM structure determination. *J. Struct. Biol.* **180**, 519–530 (2012).
56. Punjani, A., Zhang, H. & Fleet, D. J. Non-uniform refinement: adaptive regularization improves single-particle cryo-EM reconstruction. *Nat. Methods* **17**, 1214–1221 (2020).
57. Kucukelbir, A., Sigworth, F. J. & Tagare, H. D. The local resolution of cryo-EM density maps. *Nat. Methods* **11**, 63–65 (2014).
58. Emsley, P., Lohkamp, B., Scott, W. G. & Cowtan, K. Features and development of Coot. *Acta Crystallogr. D Biol. Crystallogr.* **66**, 486–501 (2010).
59. Afonine, P. V. et al. Real-space refinement in PHENIX for cryo-EM and crystallography. *Acta Crystallogr. Sect. Struct. Biol.* **74**, 531–544 (2018).
60. Sun, L. & Horrigan, F. T. A gating lever and molecular logic gate that couple voltage and calcium sensor activation to opening in BK potassium channels. *Sci. Adv.* **8**, eabq5772 (2022).
61. Marino, M., Misuri, L. & Brogioli, D. A new open source software for the calculation of the liquid junction potential between two solutions according to the stationary Nernst-Planck equation. Preprint at https://doi.org/10.48550/arXiv.1403.3640 (2014).
62. Jurrus, E. et al. Improvements to the APBS biomolecular solvation software suite. *Protein Sci.* **27**, 112–128 (2018).

Acknowledgements

This work was supported by NIH grants, R01GM143380, R01HL162842, R01GM146315, R01EY026545, and S10OD030276, and by Welch Foundation funds Q-2173-20230405 to Z.W. and Q035 to TGW. Cryo-EM data were collected at the Baylor College of Medicine Cryo-EM ATC and UTHealth Cryo-EM Core, which includes equipment purchased under the support of CPRIT Core Facility Award RP190602; SEC-MALS experiments were supported by the Biomolecular Characterization Unit, Protein and Monoclonal Antibody Production Core at Baylor College of Medicine, and the assistance of Phoebe S. Tsoi and Josephine C. Ferreon. We are deeply grateful to Ming Zhou for his insightful guidance from the inception of this Ph.D thesis project. We also extend our sincere thanks to Steven J. Ludtke and Yongcheng Song for their valuable insights and thoughtful suggestions throughout the course of this work.

Author contributions

Z.W. and F.T.H. conceived the study. Z.W., H.W., F.T.H., L.S., and T.G.W. designed the experiments. T.H. performed preliminary protein construct screenings. H.W. performed biochemistry and structural biology experiments. L.S. and H.W. performed electrophysiology experiments. All authors analyzed the results and wrote the manuscript.

Competing interests

The authors declare no competing interests.

Additional information

Supplementary information The online version contains supplementary material available at https://doi.org/10.1038/s41467-025-59678-2.

Correspondence and requests for materials should be addressed to Frank T. Horrigan or Zhao Wang.

Peer review information *Nature Communications* thanks the anonymous reviewers for their contribution to the peer review of this work. A peer review file is available.